SIMULATING OBSERVATIONS OF LOW-MASS SOURCES IN NGC 2024 WITH JWST NIRCAM

By
LAURIN MICHELLE GRAY

A Thesis Submitted to The Honors College

In Partial Fulfillment of the Bachelors degree
With Honors in

Astronomy

THE UNIVERSITY OF ARIZONA

M A Y 2 0 1 9

Approved by:

_____

Dr. Marcia Rieke
Astronomy Department

ABSTRACT

James Webb Space Telescope's (JWST) primary science imager, NIRCam, will provide near-infrared images and data with sensitivity limits never before reached, making it ideal for observing low-mass sources. In preparation for an upcoming NIRCam study of embedded cluster NGC 2024, this project constructs a possible field of view based on known sources and potential low-mass sources predicted by an initial mass function (IMF) which would have previously been unobservable, and simulates planned NIRCam observation to investigate how accurately NIRCam can observe the faint simulated objects with saturation from bright existing sources and background emission. We produced two sets of simulated sources due to uncertainties in constraining the IMF, and despite the limited time constraints, were able to evaluate the astrometric and photometric accuracy of one set of images for one set of simulated sources. We found that the extracted astrometry was accurate to within 6.3 milliarcseconds for the majority of sources and measured photometry was generally within a standard deviation of 0.06 mags, demonstrating the accuracy of the simulated observations. We also identified several areas which would benefit from a robust data analysis pipeline, such as source detection, PSF fitting, and repetition of the source simulation.

I. INTRODUCTION

The James Webb Space Telescope (JWST) is currently scheduled to launch in 2021. As the telescope's primary science imager, the Near-Infrared Camera (NIRCam) instrument will provide unprecedented observations in the 0.6-5 μm range. In preparation, we can learn more about how NIRCam will perform and what we expect it to be able to see by simulating observations. NIRCam has 5 observing modes, and two modules so it can observe in a short wavelength channel (0.6 – 2.3 μm) and a long wavelength channel (2.4 – 5 μm) simultaneously. We need to understand how far NIRCam's limits extend past previous observations. This project simulates observations of the embedded cluster NGC 2024, prepares techniques for extracting faint, low-mass sources, and evaluates how well NIRCam can reconstruct the original inputs. NGC 2024 is the subject of an upcoming Guaranteed Time Observation (GTO) program in the first cycle of NIRCam observations (Meyer et al. JWST GTO 1190). The program will attempt to observe objects down to a few Jupiter masses in size ($1\ M_{Jup} \approx 0.001\ M_{\odot}$), much lower than any previous studies of the region.

1.1. NGC 2024

NGC 2024, also called the Flame Nebula, is an active star formation region in the Orion Molecular Cloud Complex. It is about 30' x 30' in size, and is estimated to be 415 pc away from us (Anthony-Twarog 1982). It's estimated to be between 300,000 and 1 million years old (Liu et al. 2013). The GTO program will observe it with eight different filters: F070W, F115W, F140M, F182M, F277W, F300M, F335M, and F444W (Meyer et al. JWST GTO 1190). The wideband filter will disentangle intrinsic color, extinction, and detect the presence of circumstellar disk emission, whereas the medium band filters will provide evidence of water vapor and constrain surface gravity for late-type low mass objects.

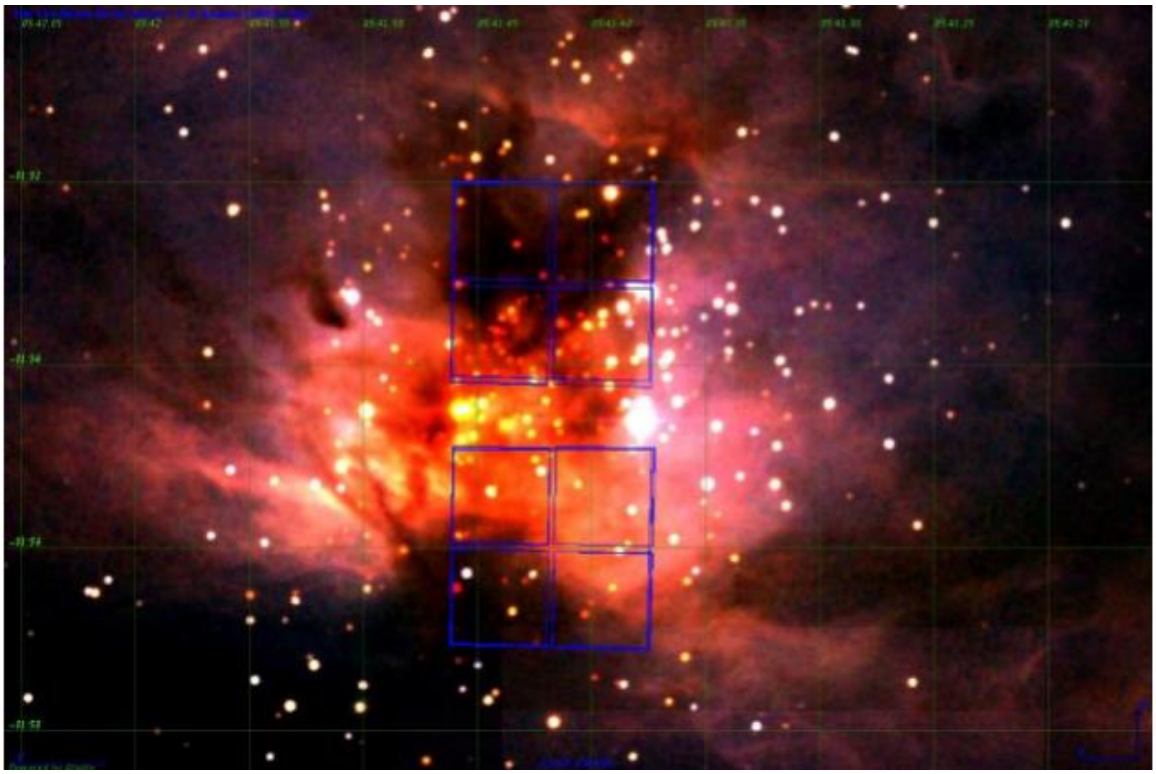

Figure 1: NGC 2024, in infrared. Observation footprints in NGC 2024 for upcoming GTO program are outlined in blue. The upper four boxes represent the area covered by the short wavelength detectors in module B, and the lower boxes show the view of the short wavelength detectors in module A.

1.2. The Initial Mass Function

The Initial Mass Function (IMF) describes the initial distribution of masses in a stellar population. Interestingly, despite predictions by current star formation theory that populations should vary based on the formation conditions, observationally, the IMF appears to be universal

(Kroupa 2002). We can assume that the present-day mass function resembles the IMF in embedded clusters like NGC 2024 because the stars are about the same age, metallicity, and distance from us – therefore, the population evolves somewhat uniformly (Dib 2014). This means that we can expect the mass distribution in NGC 2024 to follow the same shape as the IMF and use it to simulate sources. There have been several attempts to define the IMF. The one used in this project is from a 2002 paper by Kroupa. Most of the trouble comes from the shape of the low-mass end of the function. Kroupa defines "very low mass stars" as having masses between 0.072 $M_\odot$ and 0.5 $M_\odot$, and stars below 0.072 $M_\odot$ as brown dwarfs. For masses below 0.5 $M_\odot$, the IMF goes as $\xi(m) = k(\frac{m}{m_1})^{-\alpha}$, where k = 0.877 ± 0.045 stars/pc^3, m_1 = 0.08 $M_\odot$, and α = 1.3 ± 0.5 for 0.08 $M_\odot \leq m < 0.5\ M_\odot$, or α = 0.3 ± 0.7 for 0.01 $M_\odot \leq m < 0.08\ M_\odot$. The shape of the IMF is not well defined below 0.08 $M_\odot$, and especially below 0.01 $M_\odot$. In the lowest mass regime, α can range between -0.4 and 1 – and a sign change completely changes the shape of the IMF. Hence, this project will work with two potential IMFs- one where the masses follow the Kroupa defined mass function down to the Jupiter mass range (α = 0.3), and a "flat" function (α = 0) below 0.04 $M_\odot$. Figure 2 illustrates the differences between these two IMFs, with a clear break between the two at 0.04 $M_\odot$, and a subtler change in the slope at 0.08 $M_\odot$ when α changes.

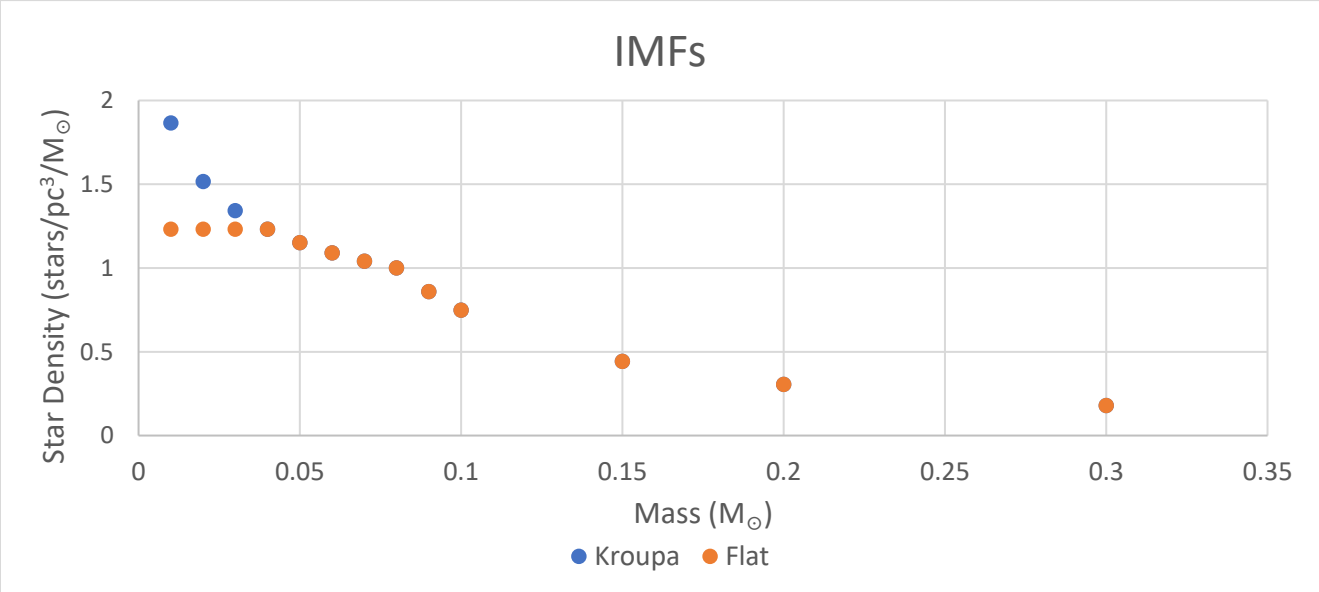

Figure 2: The mass distribution from the two IMFs- one as defined by Kroupa (2002) and one where the IMF is flat after 0.04 $M_\odot$.

II. METHODOLOGY

2.1. Known Sources

The first part of this project was creating a master catalog of sources already observed in and around the GTO footprints, which will be referred to as "known sources". I performed a search for sources within a 3' x 6.5' box centered on 5h 41m 42s, -1^{o} 54' 33", which is slightly larger than the GTO footprint area, and selected seven catalogs based on wavelength, number of sources, and goals of the survey or study. Some of these catalogs were then combined based on similarity to another catalog (coming from the same survey, or sources had already been matched). I started with sources from 2MASS (Skrutskie et al. 2006), which has JHK_s band data, and added the matching 3.6, 4.5, 5.8, 8.0, and 24 μm data from Megeath et al. (2012) (referred to as Catalog A). Similarly, I combined sources from Kuhn et al. (2013) and Broos et al. (2013), which both took data from the MYStIX program surveys and covered the same wavelengths as Catalog A (except for 24 μm) into a second catalog called Catalog B. Catalog C consists of data from Pan-STARRS Release 1 in the grizy bands (Chambers et al. 2016). Catalog D is from the DENIS survey, which has sources with J and/or K_s photometry, and sometimes I-band photometry (DENIS Consortium 2005). Catalog E is from Levine et al. (2006) which sought to spectroscopically identify low-mass objects (0.02 $M_\odot$ to 0.72 $M_\odot$) in NGC 2024 and has JHKs photometry. A summary of the catalogs is in Table 1. The number of sources refers to the number within the Vizier search area.

Table 1: Contributing Catalogs

Catalog Designation	Source(s)	Wavelengths	Number of Sources
A	2MASS & Megeath+ (2012)	JHK_s, 3.6, 4.5, 5.8, 8.0, 24 μm	219
B	Kuhn+ (2013) & Broos+ (2013)	JHK_s, 3.6, 4.5, 5.8, 8.0 μm	248
C	Pan-STARRS	grizy	287
D	DENIS	IJK_s	268
E	Levine+ (2006)	JHK_s	23

I identified Catalog A as my primary catalog, and hierarchically evaluated sources in Catalog B for their proximity to sources in Catalog A. If a source in B was within 1" of a source in A, they were treated as the same source, and any photometry not already in the catalog was added to it. If a source in B did not match any source in A, its data was added to the catalog as a new source. This created a combined Catalog AB. This process was repeated with Catalogs C, D,

and E to create the master known source catalog. Other potentially useful information such as A_V extinction or estimated classification was also included for reference. The complete known source catalog contains 585 sources with at least 2 photometric data points covering 0.4866 μm to 24 μm.

We determined that while the GTO program will observe in eight filters, we're only interested in the longest six for this project (>1.4 μm), as those are the ones where we are most likely to see the low-mass sources we're interested in. There are 256 sources in the known source catalog with J and K_s photometry, but which may or may not have H, [3.6], and/or [4.5] data. To fill in these gaps, I calculated the J-K color for all of these sources. For sources that were missing photometry, I identified the source with the closest matching J-K that did have data for the missing wavelength, calculated J-[wavelength] for that source, and used that color to estimate the missing photometry. When all of the sources had values for J, H, K_s, [3.6], and [4.5], I interpolated across those wavelengths and extracted magnitudes at the NIRCam filter wavelengths. Table 2 contains the first few rows of this catalog. The spatial distribution of these sources is displayed in Figure 3. It's important to note that these are sources that appear in the field of view, but are not necessarily within NGC 2024. They may be in front of it, or behind it. However, it is important to include them in the observation simulation because they are in the line of sight and may saturate the area around them, affecting our ability to see faint sources within NGC 2024.

Table 2: Known Sources with Photometry in NIRCam Filters

ID	RA	Dec	F140M	F182M	F277W	F300M	F335M	F444W
A1	85.4259	-1.9104	15.88	14.96	11.45	11.58	11.76	11.41
A2	85.4249	-1.9066	13.70	11.36	9.36	9.08	8.70	7.77
A4	85.4228	-1.9108	14.43	11.89	9.94	9.71	9.39	8.50
A5	85.4283	-1.9100	13.31	11.29	10.04	9.95	9.83	9.35

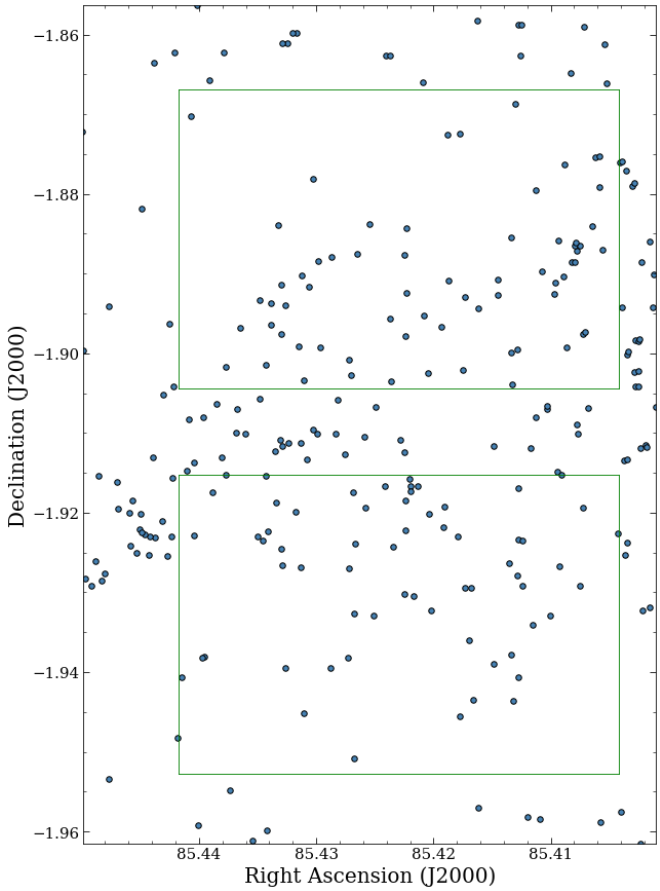

Figure 3: Spatial distribution of all sources in master known source catalog with J and K_s photometric data points. The green boxes indicate the GTO footprints from Figure 1.

2.2. "IRAC-only" Sources

There were 95 sources in my catalog that had [3.6] and [4.5] data, but no JHK_s data, which I refer to as "IRAC-only" sources. 4.5 μm is close enough to 4.44 μm that I could have included these sources in the F444W simulations, but I had no good way to extrapolate to the shorter wavelengths, so these sources would be excluded from the simulations in other filters. However, because they seem to only appear in the longer wavelengths, they were potentially some of the low-mass sources we're trying to observe. Using the AMES-Cond 2000 1 Myr isochrone models in the IRAC wavelengths as a prediction for the expected photometry for the low-mass sources, I applied the distance modulus for 415 pc and calculated [3.6]-[4.5] (Allard et al. 2001). I dereddened my IRAC-only sources using my extinction map (section 2.4) and calculated [3.6]-[4.5] for those sources as well. If the IRAC-only sources represent some of the low-mass sources we're looking for, we would expect correlation on a [3.6] vs. [3.6]-[4.5] color-

magnitude diagram (CMD), since both are dereddened and in apparent magnitudes. However, when these sources were plotted with the model (as seen in Figure 4), there was a wide scatter of IRAC-only sources compared to the line of model sources. There's likely red-excess emission involved in the photometry of the sources to the right of the model line, probably due to the presence of a circumstellar disk, and the simulation doesn't account for disk emission from sources. The majority of the IRAC-only sources were brighter than expected for the low-mass sources we're simulating (<0.04 $M_\odot$), so we conclude that these are not the low-mass sources we're looking for, and exclude them for the sake of consistency for all the wavelength simulations.

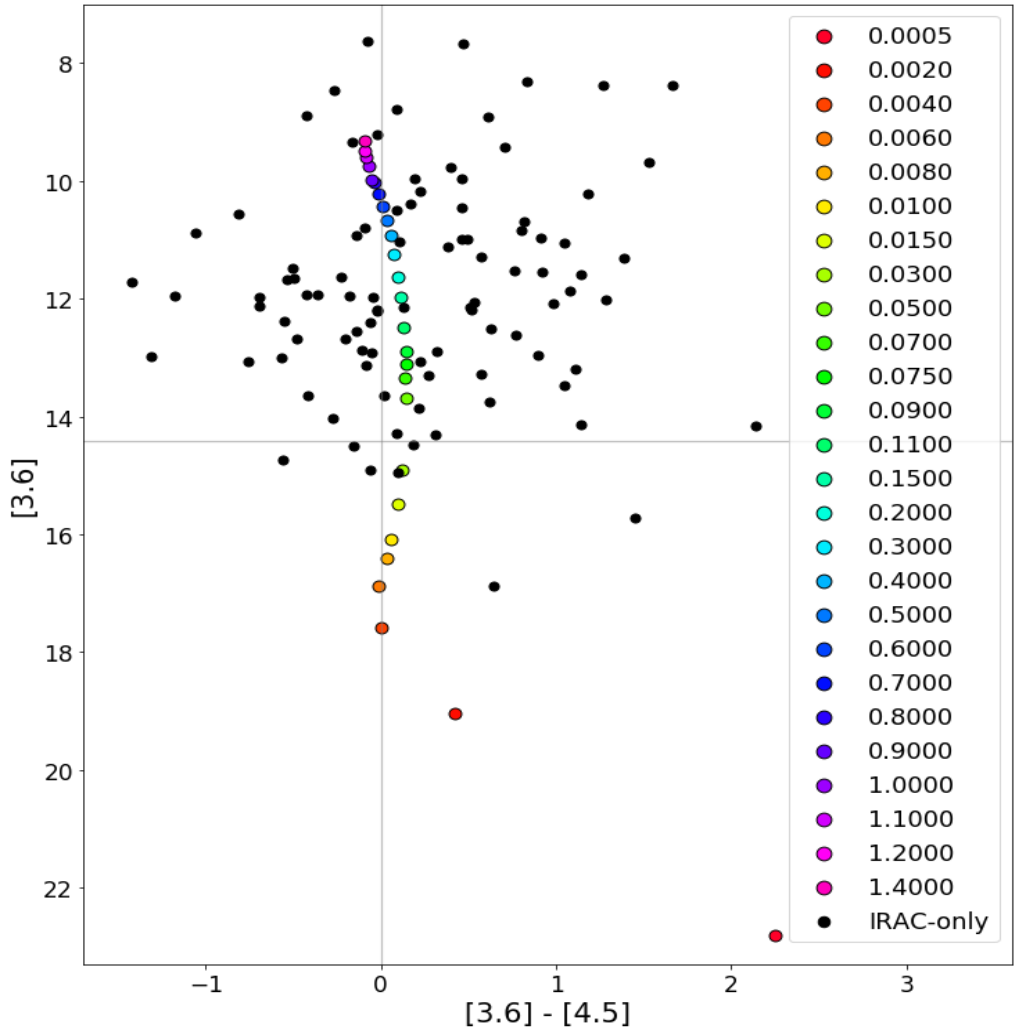

Figure 4: CMD comparison of IRAC-only sources (after dereddening) to model photometry (with distance modulus). The masses are in units of $M_\odot$. The vertical grey line marks a color of zero, and the horizontal line shows the [3.6] magnitude of a 0.04 $M_\odot$ source. Only seven sources out of 95 fall below that line (lower mass).

2.3 Simulation of Low-Mass Sources

In order to simulate sources to match the IMF for a region, it's important to have an idea of the already identified existing population. Levine et al. (2006) estimated the mass and spectral type of 67 low-mass sources in NGC 2024 using spectroscopic analysis, with a larger field of view than my master catalog. They estimate their mass completeness fraction at about 35%, and a mass completeness limit of 0.04 $M_\odot$. Using their count of 6 sources with masses of 0.04 $M_\odot$, I therefore estimated that there should be about 17 sources with mass 0.035 $M_\odot$ to 0.045 $M_\odot$. This was used to scale the integral of the IMF over the same interval, and the scaling factor applied to the mass distribution below 0.045 $M_\odot$ to find the expected numbers of stars in this mass range. This method estimates that there should be 101 objects with masses 0.04 $M_\odot$ and below with the Kroupa IMF, and 76 objects in the same mass range for the flat IMF. Note that objects above 0.04 $M_\odot$ will not be simulated, because that was the completeness limit. The full counts for mass ranges in both IMFs can be found in Table 3. These can be broken down into smaller ranges to allow for a larger variety of mass values, based on the available mass values in the low-mass model. The numbers of sources to be simulated are rounded, since I can't simulate a partial object. The actual numbers of simulated stars excludes known sources; for example, because I already know about 6 sources in the 0.04 $M_\odot$ range, I only needed to simulate 11 sources of mass 0.04 $M_\odot$ to reach the full expected count of 17.

Table 3A: IMF Mass Bins, Kroupa

Bin Midpoint ($M_\odot$)	**Bin Min ($M_\odot$)**	**Bin Max ($M_\odot$)**	**Integrated & Scaled IMF**	**Number to Simulate**
	0.0005	0.005	18.272	18
0.01	0.005	0.015	26.426	26
0.02	0.015	0.025	21.172	20
0.03	0.025	0.035	18.703	9
0.04	0.035	0.045	17.143	11

Table 3B: IMF Mass Bins, Flat

Bin Midpoint ($M_\odot$)	Bin Min ($M_\odot$)	Bin Max ($M_\odot$)	Integrated & Scaled IMF	Number to Simulate
	0.0005	0.005	7.714	8
0.01	0.005	0.015	17.143	17
0.02	0.015	0.025	17.143	16
0.03	0.025	0.035	17.143	7
0.04	0.035	0.045	17.143	11

I used AMES-Cond 2000 1 Myr isochrone models in the six JWST NIRCam filters to obtain absolute Vega magnitudes for my simulated sources, and created the needed numbers of each mass range for both IMFs (Allard et al. 2001). I then randomly scattered these sources within the Levine field of view, checked that none of my simulated sources fell within 1" of any known sources (or they would have been counted as the same source if they were actually observed), and identified the sources that fell within the smaller field of view of my full known source catalog. It didn't matter if simulated sources from the two IMFs happened to fall near each other, because they are separate cases. In all, I ended up with 20 sources in my Kroupa catalog, and 15 sources in my flat catalog. The spatial distribution of both sets of sources is in Figure 5, and the numbers for each mass are in Table 4. I retrieved A_V for each simulated source coordinate from my extinction map, converted the extinction to each NIRCam filter wavelength (section 2.4), and added them to the appropriate photometry after applying the distance modulus of 415 pc to get the apparent magnitudes.

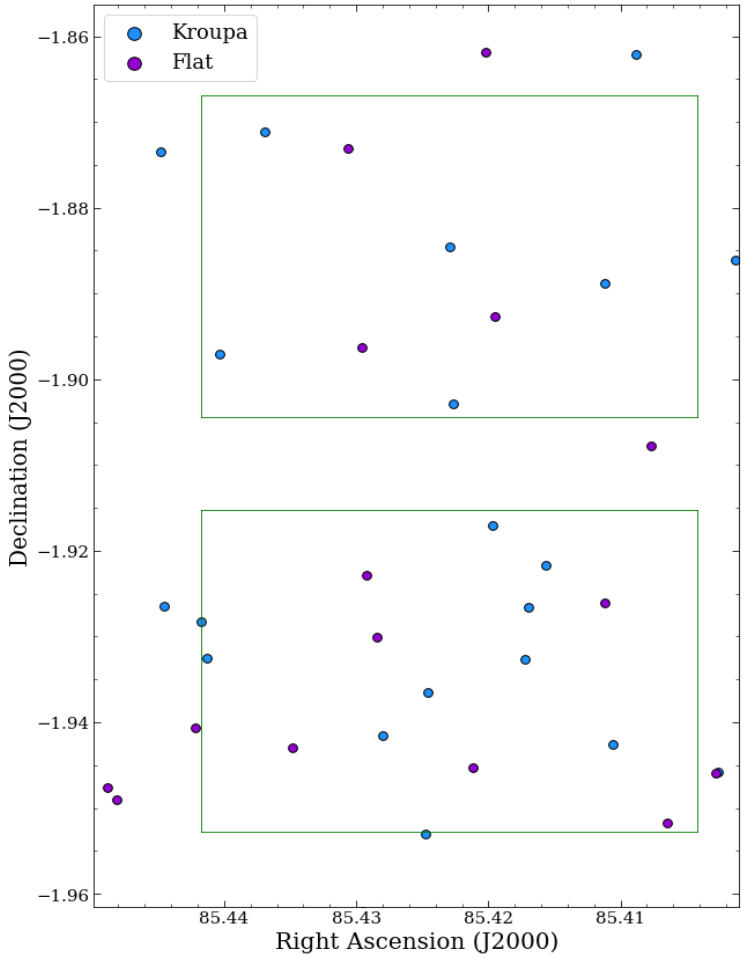

Figure 5: Spatial distribution of Kroupa (blue) and flat (purple) IMF sources in my field of view.

Table 4: Simulated Sources in Field of View

Mass ($M_\odot$)	**Kroupa Number**	**Flat Number**
0.0005	1	0
0.001	2	0
0.002	0	1
0.003	1	0
0.006	1	1
0.007	2	1
0.008	0	1
0.009	1	0
0.01	1	1
0.015	4	1
0.02	4	1
0.03	2	3
0.04	1	5
Total	**20**	**15**

2.4. Extinction Mapping

Some of the sources from the Broos et al. (2013) catalog have values for A_V associated with them, which can be used to estimate the extinction over the entire field of view by fitting a surface to the known data with the scipy package griddata, which performs a cubic spline interpolation between a set of non-uniform grid data. However, it doesn't extrapolate beyond the outermost sources, so I queried in Vizier with a larger field of view (5' x 8.6') than the master known catalog field of view to make sure that the entire catalog area was included in the map. This fitted surface can be seen in Figure 6. Extinction values range from 2.004 to 55.81 across the known master catalog field of view. An extinction value in V-band can be converted to extinction in another wavelength λ using the Rieke & Lebofsky (1985) extinction laws. The relations follow a power law of $\frac{A_\lambda}{A_V} = 0.3773\lambda^{-1.655}$, between 0.651 μm and 4.75 μm, so A_λ at any point can be calculated for each of the NIRCam filters by getting A_V at that point and solving the power law.

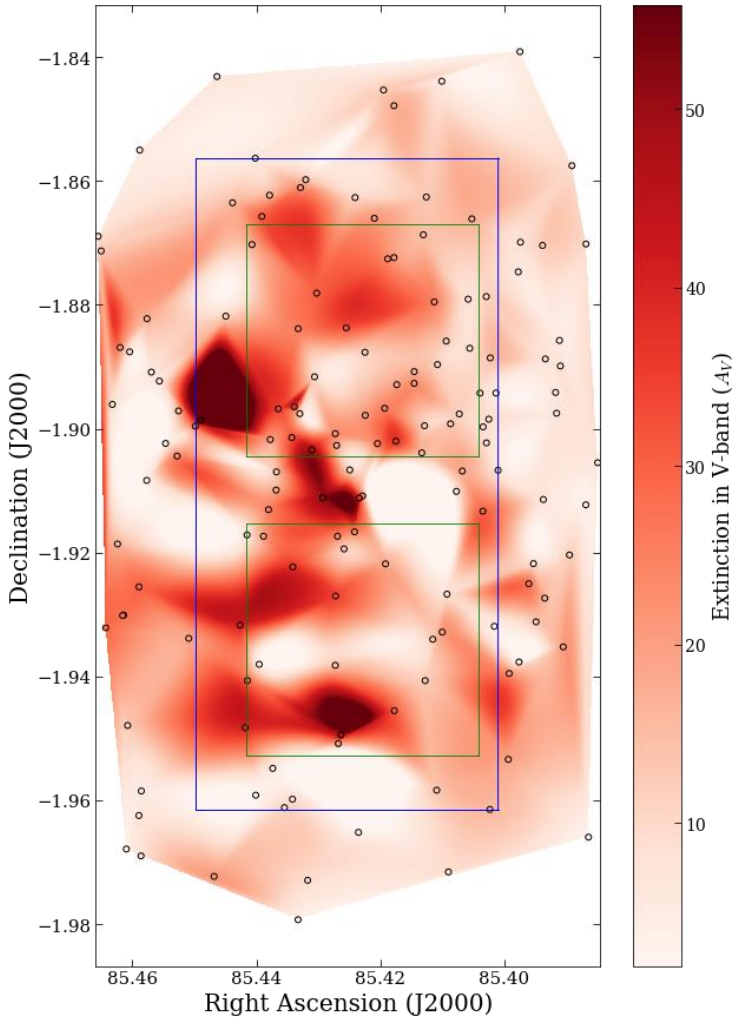

Figure 6: Normalized surface fit of A_V. The blue rectangle indicates the field of view of the master known source catalog while the green rectangles designate the GTO observation footprints in Figure 1. The circles represent the A_V data points that the surface was fit to- when the circle color is close to the color of the area surrounding it, it indicates an accurate fit nearby.

2.5. Nebular Emission

To estimate the background nebular emission, we first obtained Wide-field Infrared Survey Explorer (WISE) data of NGC 2024 (Wright et al. 2010). Using astropy photutils[1], we identified and removed prominent bright sources, which should already be included in the master source catalog. The background at each source position was interpolated from the surrounding extended emission. The resulting WISE W1 and W2 background images were converted from

[1] https://photutils.readthedocs.io

raw units to Jy/pixel according to the WISE Data Manual[2]. The flux was subsequently re-binned to match the pixel sizes for NIRCam, and then converted from Jy to photons/sec/cm^2/A for each pixel in the catalog field of view. To determine the image count rate for a given NIRCam filter, the W1 and W2 bands were linearly extrapolated NIRCam filter's central wavelength, and the result multiplied by the filter bandpass and JWST collecting area. Figure 7 contains the resulting nebular emission in the six NIRCam filters. The plots are all scaled to the same range, so it's apparent that emission increases at longer wavelengths.

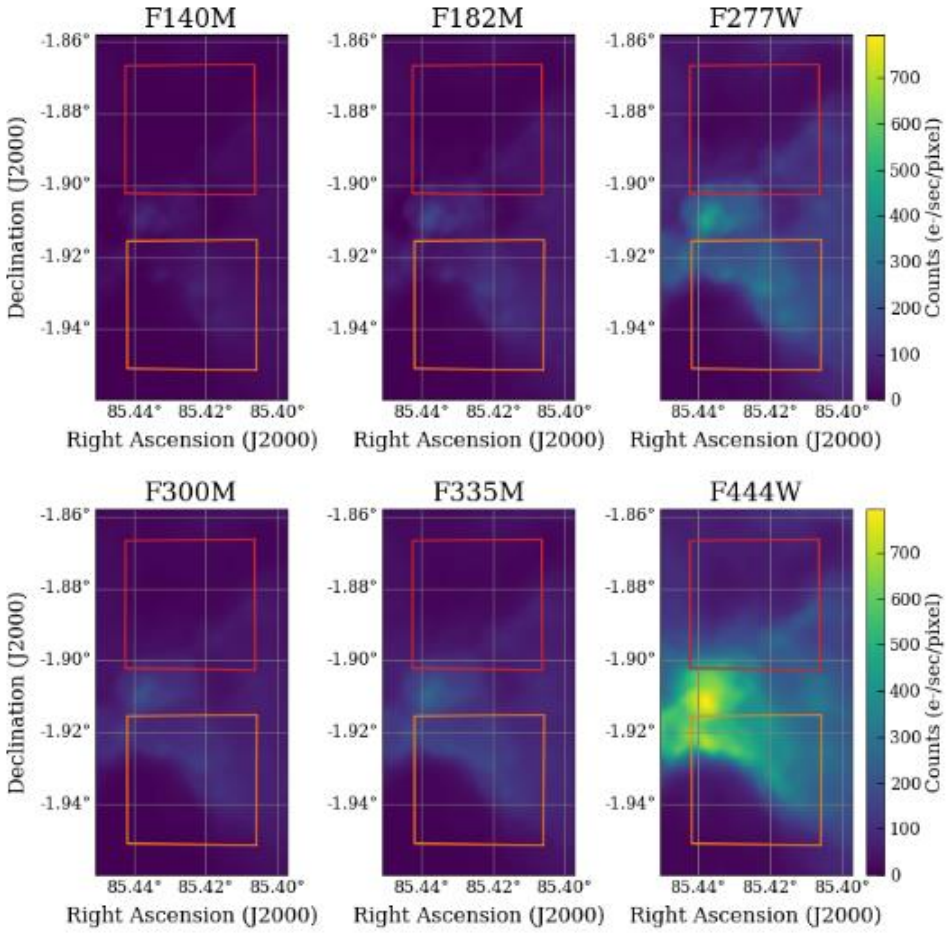

Figure 7: Nebular emission, in 6 NIRCam filters, in units of photons/second/pixel. The orange and red boxes mark the GTO footprints for modules A and B, respectively.

[2] http://wise2.ipac.caltech.edu/docs/release/allsky/expsup/sec2_3f.html#tbl1

2.6. Observation Simulations

Observations were simulated for 6 NIRCam filters, with corresponding detectors (Table 5), in 16 dither position for each filter/detector pair, with 4 integrations in each position. My catalog field of view is larger than the observation footprints, so the simulations are able to include light from sources just outside the image, which have point spread functions (PSFs) that may affect the image. The simulated sources were input into a simulation program called Guitarra[3] written by Dr. Christopher Willmer (Willmer et al., in prep). The simulation includes detector structure, kTC noise, read noise, pixel non-linearities, and photon flux. This software was written for extragalactic observations of very faint objects, and so it ray-traces all photons individually. Due to this, our catalog of known sources tended to be too bright for Guitarra to handle in a reasonable amount of time, especially for the short timescale of an undergraduate thesis project. The bright sources were instead simulated using pynrc[4] functions written by Dr. Jarron Leisenring (Leisenring et al., in prep). The pynrc simulation includes nebular emission, but no other sources of noise except for photon noise, because the detector-related noise was already accounted for in Guitarra.

Table 5: Detectors Associated with each NIRCam Filter

Filters	**Detectors**
F140M, F182	481/A1, 482/A2, 483/A3, 484/A4, 486/B1, 487/B2, 488/B3, 489/B4
F277W, F300M, F335M, F444W	485/A5, 490/B5

The output ramps of each simulation were added together, so that we had a set of observations of known sources combined with each set of simulated sources. We performed a linear fit to each pixel in an image to get the slope in units of ADU/second, and replaced saturated pixels with NaN values to flag them. In future simulations and for actual data, we would use a pipeline that would be able to account for pixel non-linearities as well as proper bias and dark calibrations. We then median combined all slopes for each dither position in order to get an average slope so that I could perform photometric measurements. In the future, we would combine these slopes into a single image using a mosaicking method such as AstroDrizzle[5],

[3] https://github.com/cnaw/guitarra
[4] https://pynrc.readthedocs.io/
[5] http://drizzlepac.stsci.edu/

which will allow for deeper point source detection, but for now we have 16 slope files for each detector (one for each dither position. Figure 8 shows the images produced at each part of this process, for a single detector (485/A5) at dither position (1) of the F444W filter. The simulated sources are from the Kroupa IMF.

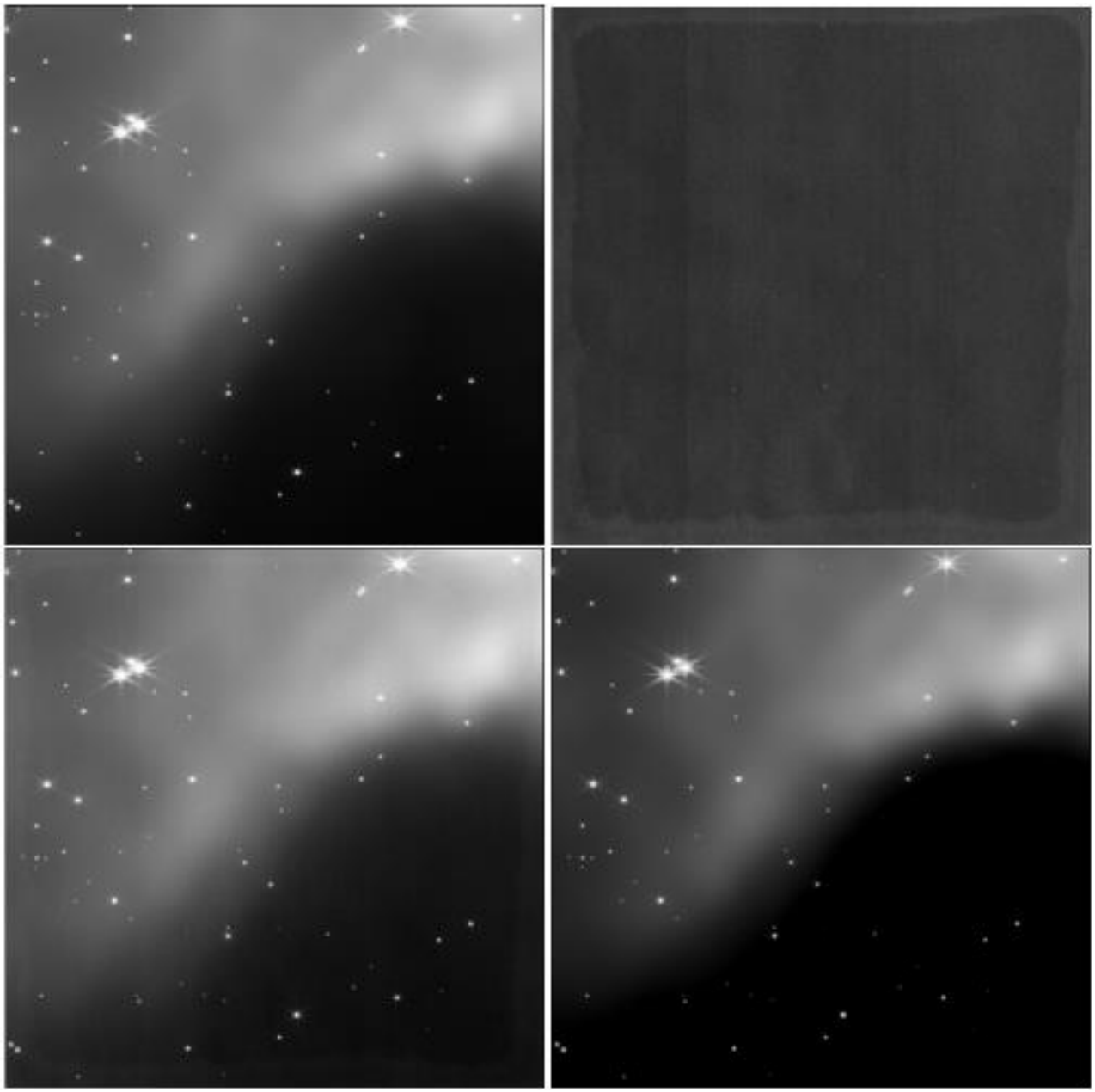

Figure 8: Top left: Known sources and nebular emission, produced by pynrc simulation. Top right: Kroupa simulated sources, produced by Guitarra simulation. They are so dim, they're barely visible on top of the detector bias noise in the image. Bottom left: combination of top left and top right images. Bottom right: Slope image from combined image ramps. The first three images are all the first integration, fully exposed.

III. DATA ANALYSIS

Due to time constraints, we were only able to perform preliminary photometric analysis for the Kroupa IMF on a single filter. We chose F444W because as a wide, long wavelength filter, it should provide the best sensitivity to the simulated low-mass sources, while being less susceptible to line-of-sight extinction within the cluster. Additionally, the F444W detectors cover the largest spatial area, which maximizes the number of simulation sources in the observation area that we can perform photometric analysis on.

We did not have time to investigate software algorithms to detect faint low-mass sources without location input. Blind detection of low-mass sources is complicated by the spatially variable background and numerous saturated regions from bright sources. Additionally, the bright diffraction spikes confuse many algorithms into treating each spike as a separate source. One potential technique to combat these issues is to explore an image by breaking it into subsections (64 x 64 pixels, for example), fitting a 2D background, and then searching that region for unsaturated sources with a peak-finding algorithm. For the time being, we will use the known positions of the simulated sources as though they were retrieved with a procedure that successfully identified our input sources without false positives.

For each of our slope images we cut out a 64 x 64 pixel subsection centered on the identified sources and perform a 2D background subtraction, masking out the source. We used a linear least-squares fitting routine to fit a theoretical PSF of a 0-mag star to the background subtracted image, resulting in a best-fit subpixel position along with the scale factor that would minimize the residuals. This scale factor translates directly to the final observed magnitude as mag = -2.5*log(scale). The fitting routine uses a Fourier image shift to adjust the theoretical PSF in order to obtain subpixel precision. This procedure was applied to all simulated sources in each slope image. The final magnitude for a source was calculated by averaging the measurements from all of the positions it appears in, with the standard deviation giving the uncertainty.

IV. RESULTS

4.1. Astrometric Accuracy

With the exception of one source, the retrieved positions are within $1/10^{th}$ of a pixel, or about 6.3 milliarcseconds (mas), of their input positions. Fainter sources tend to have larger

offsets and higher PSF fit variance. The majority of sources appear to clump around a systematic offset of (0.06, -0.05), with a standard deviation of 0.02 pixels, about 1.3 mas (Figure 9). These offsets may be an artefact of the PSF fitting algorithm, or a result of the discrete nature of the simulated PSFs; the PSFs themselves do not have infinite resolution, and these offsets may be the limit of that resolution. The offsets could also be due to slight differences in the shape of the simulated PSFs compared to the theoretical PSF used to fit the source position.

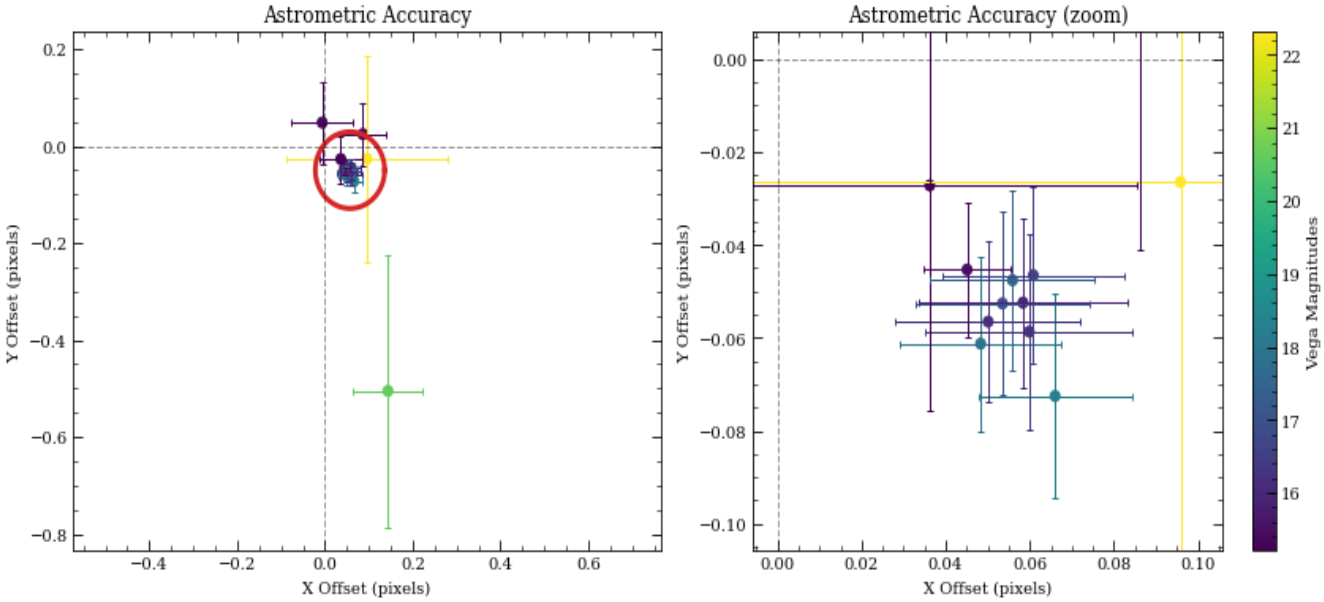

Figure 9: Plots showing the astrometric accuracy. Left: X and Y differences (in pixels) of the input stellar locations minus the extracted center position. The color scale shows that fainter sources tend to have higher uncertainties in their astrometric fits. The red circle indicates a clump of source that are systematically offset from their true locations. Right: Same as the left plot, but zoomed into the clump to better show the relative differences. The standard deviation of that clump is 0.02 pixels, or approximately 1.3 mas.

4.2. Photometric Accuracy

Overall, the magnitudes we were able to retrieve from the simulation agree very well with the input magnitudes. Table 6 shows the input and output magnitudes, in Vega magnitudes, for each of the 15 sources from the Kroupa catalog that appeared in at least one dither position of one detector. The output magnitude is the average of all the magnitudes extracted for that source, and the uncertainty is the standard deviation of that set of magnitudes. The average difference between input and output magnitudes was 0.009 mags, with a standard deviation of 0.06 mags for the differences. Figure 10 is a plot of the differences against the input magnitudes. It shows that the differences tend to scatter around 0 and that as expected, the uncertainty for the

extracted magnitude was higher on fainter sources. However, the signal-to-noise ratio (SNR) appears to plateau for brighter sources with fluxes greater than 40 μJy (≈ 16.6 Vega mag), rather than scaling by the square root of the flux as expected (Figure 11). This requires further investigation to determine if this is an artefact of the simulation or the processing method, but it may be due to systematic uncertainties in the PSF fitting routine which mean we're not reaching the photon limit.

Table 6: Comparison of Input and Extracted Photometry for Simulated Sources (Kroupa IMF)

Source ID	**Mass ($M_\odot$)**	**F444W, Input (Vega mag)**	**F444W, Output (Vega mag)**	**Uncertainty (mags)**
257	0.0005	22.31	22.41	0.180
258	0.001	20.59	20.62	0.067
260	0.003	18.25	18.17	0.019
261	0.006	16.93	16.87	0.024
262	0.007	17.94	17.86	0.023
263	0.007	17.45	17.51	0.023
264	0.009	16.59	16.67	0.021
265	0.01	16.22	16.17	0.020
266	0.015	16.16	16.24	0.027
267	0.015	15.91	15.87	0.022
270	0.02	15.43	15.36	0.016
272	0.02	15.21	15.17	0.041
273	0.02	15.33	15.31	0.047
276	0.04	15.35	15.40	0.038

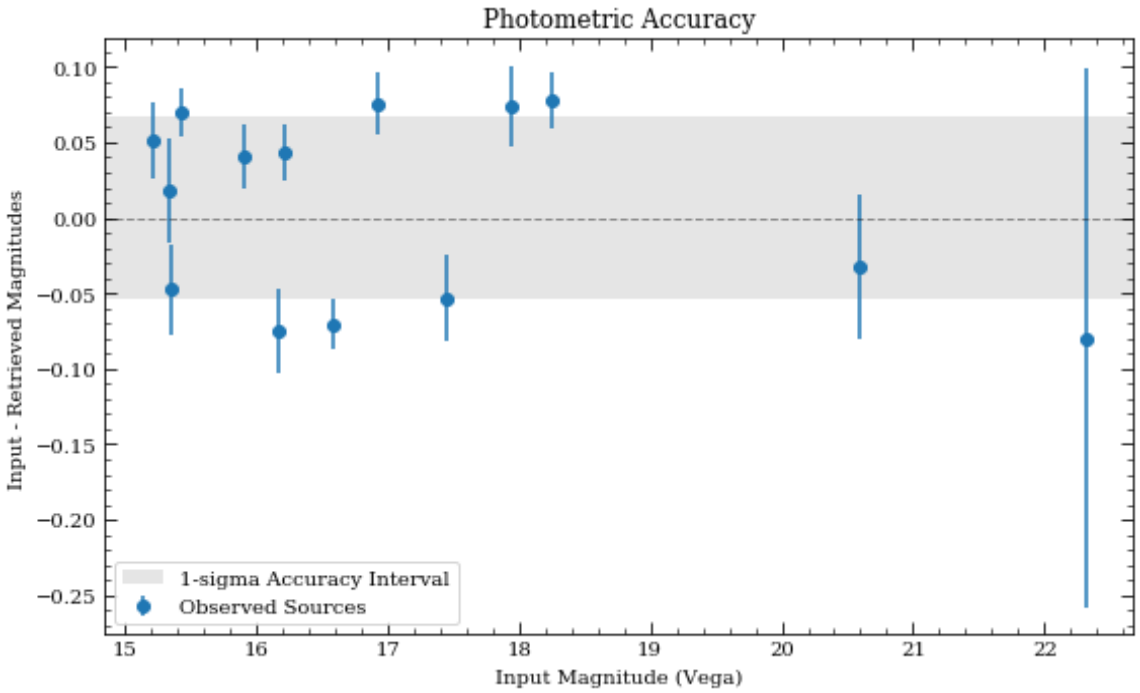

Figure 10: Plot of the difference between the input and retrieved magnitudes with respect to the input brightness. This plot indicates that we can reliably obtain the correct stellar fluxes within the measured uncertainties.

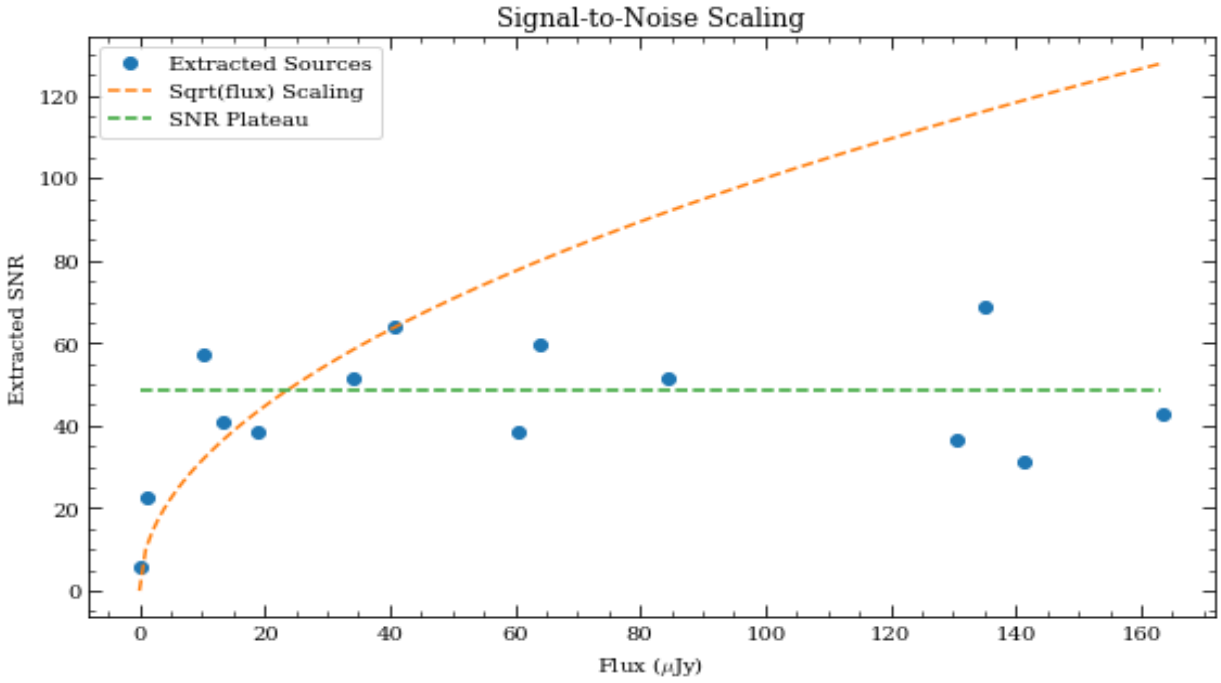

Figure 11: The extracted signal-to-noise ratio for the sources (blue dots) roughly follows a sqrt(flux) scaling (orange dashed line) until 40 μJy, when the SNR unexpectedly flattens out to an average of about 49 (green dashed line).

V. DISCUSSION

5.1. Simulation Accuracy

The simulated source populations are entirely dependent on the mass estimations of Levine et al. (2006), which was a relatively small sample size (67 sources), and is heavily affected by their uncertainties. For example, if I had chosen a different mass range to scale my IMF to, or used a more conservative completeness fraction (they estimated a range from 30%-40%), my simulated source counts would be different. I did compare the average magnitude and J-K color (after dereddening based on their estimated extinction) of each Levine spectral type to my other known sources, but the Levine spectral "standards" didn't follow an expected progression of dimmer & redder with decreasing mass, making it difficult to use as a baseline for evaluating the population of the rest of my sources. When I did the same comparison with spectral type standards from an unpublished table from a 2013 paper by Pecault & Mamajek[6], almost all of my known sources were too bright to be considered M-dwarfs, indicating that the majority of my known sources are higher mass, which is expected.

Additionally, the distribution of the simulated sources was randomized, meaning that there are regions where no simulated sources were positioned. If we were to repeat the simulation with different scatterings of simulation sources, the lowest limit in one simulation might be different in another, if those sources fall closer to a bright source or in an area of higher background emission, or if none of them fall into the field at all. As such, to truly gain an understanding of NIRCam's observational limits, we would repeat the simulation source scattering and subsequent analysis multiple times.

5.2. IMF Distinction

Ideally between the counts of the sources I extract, I should be able to tell the difference between the two IMFs (for example, if I observe 2 or more simulated sources corresponding to 0.04 $M_{\odot}$, I'll know I'm looking at the flat IMF, because only one source of that mass fell in the field for the Kroupa simulation). If I had chosen to scale my IMFs down to my field of view as a fraction of the Levine field of view (about 0.236) before adding the simulation sources, the IMFs would be indistinguishable by count until I reached around 0.02 $M_{\odot}$. However, this would

[6] http://www.pas.rochester.edu/~emamajek/EEM_dwarf_UBVIJHK_colors_Teff.txt

assume a perfect scattering, which isn't the case in reality- even in the Levine sample, half of the known 0.04 $M_\odot$ sources fall into my field of view. The difficulty in distinguishing IMFs despite significant differences in the source counts in Table 3 as the bin midpoints decrease is due to the small size of the field of view. For example, in the 0.01 $M_\odot$ bin, there are 26 simulation sources for the Kroupa IMF and only 17 for the flat IMF, across the entire Levine field of view. However, when proportioned to my field of view, there would be 6 simulation sources in the Kroupa IMF and 4 in the flat IMF. Given the high amount of emission in some filters, the ability to observe sources at this mass would heavily depend on their distribution; we might detect 4 sources in both simulations, because 2 of the Kroupa sources are near a bright source or in a high emission area. Or we might detect 3 sources in the Kroupa simulation and 4 in the flat simulation, and if we didn't know which one was which, we would expect the Kroupa simulation to have more sources. The distinction between the two IMFs becomes clearer as we're able to observe lower mass sources, which is why it's imperative that we understand NIRCam's sensitivity limits.

5.3. Further Work

The next step in this project would be to complete photometric analysis and compare the photometry I was able to extract to what I put into the field for all of the images. Between the two sets of simulations, I should be able to get an upper limit of NIRCam's sensitivity. In the future, we would want to create more robust pipelines for generating slope images and detecting sources, in order to obtain more accurate photometry. With the full set of photometry, we can put limits on our ability to determine the intrinsic spectral energy distributions (SEDs) and determine masses, effective temperature, and surface gravity of these sources.

To further refine the sensitivity estimate, we could redistribute the simulation sources and repeat analysis several more times to mitigate the effects of proximity to bright sources and bright background emission. Running a series of Monte Carlo simulation in this way would provide a range of uncertainties in how well we can probe the cluster's IMF. We would be able to estimate an average observation limit based on the results from multiple simulations, and a "best case scenario" from the lowest mass observed across all simulations.

This simulation also assumed the simplest cases- single star systems, with no extended emission. We would want to improve the simulation by accounting for circumstellar disk

emission, binary systems, and different atmospheric models. We could also include the possibility of giant planets that have been ejected through dynamical interactions, since the goal sensitivity is so high, and investigate the effects of contamination by older (background) stars that are not members of the cluster. Levine et al. (2006) even identified two potential background giants as part of their sample.

ACKNOWLEDGEMENTS

Thank you to Dr. Marcia Rieke & Dr. Jarron Leisenring for their guidance and expertise during this project.

Thank you to Dr. Christopher Willmer for the use of his observation simulator, Guitarra. Guitarra is available at https://github.com/cnaw/guitarra.

This publication makes use of data products from the Two Micron All Sky Survey, which is a joint project of the University of Massachusetts and the Infrared Processing and Analysis Center/California Institute of Technology, funded by the National Aeronautics and Space Administration and the National Science Foundation.

This publication also makes use of data products from the Wide-field Infrared Survey Explorer, which is a joint project of the University of California, Los Angeles, and the Jet Propulsion Laboratory/California Institute of Technology, funded by the National Aeronautics and Space Administration.

REFERENCES

Allard, F., et al. 2001, ApJ, 556, 357

Anthony-Twarog, B. J. 1982, AJ, 87, 1213

Broos, P.S., et al. 2013, ApJ, 209, 32

Chambers, K. C., et al. 2016, Pan-STARRS1 Surveys, arXiv, 1612, 05560

Comerón, F., Rieke, G. H., & Rieke, M. J. 1996, ApJ, 473, 294

DENIS Consortium 2005, VizieR Online Data Catalog, BDENIS

Dib, S. 2014, MNRAS, 444, 1957

Kroupa, P. 2002, Science, 295, 82

Kuhn, M. A., Povich, M. S., Luhman, K. L, Getman, K. V., Busk, H. A., & Feigelson, E.D. 2013, ApJ, 209, 29

Leisenring, J., et al. 2019, in preparation

Levine, J. L., Steinhauer, A., Elston, R., & Lada, E. A. 2006, ApJ, 646, 1215

Liu, W., Meyer, M., Cotera, A., & Young, E. 2003, AJ, 126, 1665

Megeath, S.T., et al. 2012, AJ, 144, 192

Meyer, M., et al., JWST GTO proposal 1190, http://www.stsci.edu/jwst/phase2-public/1190.pdf

Pecault & Mamajek 2013, ApJS, 208, 9P

Rieke, G. H., & Lebofsky, M. J. 1985, ApJ, 288, 618

Skrutskie, M.F., et al 2006, AJ, 131, 1163

Willmer, C., et al. 2019, in preparation

Wright, E. L., et al. 2010, AJ, 140, 1868